Chitosan/WS$_2$ nanosheets co-assembled aerogels with anisotropic micro-channels for efficient Pb(II) adsorption

Yanhao Yuan[a,b,†], Xiangsheng Han[a,b,†], Hongzhen Cai[a,b,*], Keyan Yang[a,b], Feng Gao[c], Chengqian Jin[a,b,*]

[a]School of Agricultural Engineering and Food Science, Shandong University of Technology, Zibo 255000, China,
Tel. +86 0533-2786398; emails: chzh@sdut.edu.cn (H. Cai), 412114402@qq.com (C. Jin), yyhyyh994994@163.com (Y. Yuan),
hanxs@sdut.edu.cn (X. Han), ykysdut@163.com (K. Yang)
[b]Shandong Research Center of Engineering and Technology for Clean Energy, Zibo 255000, China
[c]Zibo Energy Research Institute, Zibo 255000, China, Tel. +86 0533-2926770; email: gfeng1976@126.com (F. Gao)

ABSTRACT

Building aerogels-based adsorbents with high adsorption capacity, selectivity, and structure designing through green and simple ways was urgent issue for the removal of Pb^{2+} from contaminated water. In this study, for the first time, chitosan was applied as assistant agents for the liquid-phase exfoliation of WS$_2$ nanosheets, and the composite aerogels (CS/WS$_2$) with oriented microchannel structures were obtained *via* directional co-assembly processes. Owing to the potential H-bond between CS and WS$_2$, as well as the sulfur-rich surfaces, CS/WS$_2$ aerogels exhibited promising Pb^{2+} adsorption performance (~275.9 mg/g) than many other chitosan-based adsorbents. Besides, the adsorption of Pb^{2+} by CS/WS$_2$ aerogels were also rapid (reached an equilibrium at ~120 min), selective (~54% of maximal Pb^{2+} uptake), and sustainable (maintained ~90% of the maximal uptake). This work paved a simple and green way to construct WS$_2$ nanosheets-based aerogels with delicate micro-structures and favorable Pb^{2+} adsorption performances.

Keywords: Transition-metal dichalcogenides; Chitosan; Aerogels; Anisotropic micro-channels; Pb^{2+} adsorption

1. Introduction

Water pollution caused by Pb^{2+} is gaining great attentions due to its high toxicity, non-biodegradability and tendency to accumulate through food chain, which eventually threatens human health (e.g., binding to proteins in living organisms and inhibiting their functions) and ecological balance (e.g., accumulating in soil and affecting plant growth) [1,2]. In the past few decades, various Pb^{2+} removal methods have been developed, including biological treatment [3], membrane separation [4], ion exchange [5], chemical reduction [6], and advanced oxidation processes [7], which still suffer from drawbacks like low efficiency, high costs, and potential chemical consumption [8–10]. In contrast, adsorption that using clay, carbon-based materials, zeolite and polymers as adsorbents is considered as promising strategy for the remediation of Pb^{2+} contaminated water due to its high performance, low cost and simple operation process [11–13].

Recently, transition-metal dichalcogenides (TMDs, e.g., WS$_2$ and MoS$_2$) with sulfur rich surfaces that can specifically interact with Pb^{2+} through strong Lewis acid-base soft-soft interactions, are becoming the perfect adsorbents for Pb^{2+} adsorption [14]. Typically, bulk TMDs are composed of monolayers which consist of strong covalently

---

* Corresponding authors.
† Yanhao Yuan and Xiangsheng Han are co-first authors.

bonded atomic tri-layers of sulfur-transition metal-sulfur, and stack by weak van der Waals force between neighboring monolayers [15]. Considering that the free spacing between neighboring layers is small (e.g., 0.3 nm for MoS_2), mono- or several-layered transition-metal dichalcogenides nanosheets (TMDNs) with high surface areas and abundant exposed sulfur atoms are prepared by mechanical cleavage, chemical vapor deposition, ion intercalation, or liquid-phase exfoliation [16,17]. To be noted that the obtained TMDNs are always composited with polymer matrix to form aerogels in order to avoid the agglomeration issue of nanoscale TMDNs in water [18]. However, the preparation of TMDNs are always low efficient, and the construction of TMDNs-based composite aerogels are also complicated and lack of structural designing.

Chitosan (CS, poly-β-(1→4)-2-amino-2-deoxy-D-glucose), produced by alkaline deacetylation of chitin (e.g., in the shells of shrimp and crab), is one of the most abundant and renewable polysaccharides on earth, which can be the perfect choice for the construction of TMDNs-based aerogels [19,20]. At first, chitosan is rich in amino and hydroxyl groups, which can bind to the surfaces of TMDNs *via* non-covalent interactions (e.g., H-bond and electrostatic attracting), reduce the surface free energy of TMDNs, and facilitate their liquid-phase exfoliation. Secondly, chitosan can easily crosslink by the deprotonation behavior of hydroxide ion on its polymer chain and form highly porous aerogels after freeze-drying [21]. At last, as natural polysaccharides with plenty of amino and hydroxyl groups, chitosan is also promising for the adsorption of Pb^{2+} through mainly chelating interactions, which might provide synergetic removal performance of Pb^{2+} from waste water by its composite aerogel [22].

Herein, in this study, for the first time, chitosan was applied as assistant agent for the liquid-phase exfoliation of WS_2 nanosheets and the construction of composite aerogels. The CS/WS_2 aerogels (CS/WS_2) with oriented microchannel structures were fabricated *via* simple co-assembly processes and applied for the removal of Pb^{2+} from wastewater. Owing to the three-dimensional anisotropic porous structure and sulfur-rich surfaces, the CS/WS_2 aerogels exhibited promising Pb^{2+} adsorption performance (~275.9 mg/g), which was higher than many chitosan-based adsorbents reported in the literatures. Besides, the adsorption of Pb^{2+} by CS/WS_2 aerogels were also rapid (reached an equilibrium at ~120 min) and selective (maintained ~54% of the maximal Pb^{2+} uptake).

2. Materials and methods

2.1. Materials

Chitosan with a deacetylation degree of 80%–95%, lead nitrate, ethylenediaminetetraacetic acid disodium salt (EDTA-2Na), cadmium nitrate and cupric nitrate were purchased from Sinopharm Chemical Reagent Co., Ltd., (China). WS_2 was obtained from Sigma-Aldrich. Glacial acetic acid was from Shanghai Macklin Biochemical Co., Ltd., (China). Sodium hydroxide was supplied by Yantai Shuangshuang Chemical Co., Ltd., (China). Ultrapure water (resistivity: 18.2 MΩ/cm) was utilized for all the aqueous solutions.

2.2. CS assisted liquid-phase exfoliation of WS_2 nanosheets

Briefly, certain amount of chitosan (0.01, 0.05, 0.1, 0.25, 0.5, 1, 1.5, 2, 3, 4, 5, and 6 g) was dissolved in 100 mL of 5 wt.% acetic acid solutions, and stirred at room temperature for 6 h. Then, bulk WS_2 was added to chitosan solution at an initial concentration of 5 mg/mL and treated by ultrasonic crusher (Tianhua, TH-70BQX, China) with a power of 700 W at 25°C for 8 h. The mixture was centrifuged at 3,000 rpm for 10 min to remove bulk WS_2, and the supernatant was retained as CS/WS_2 dispersion.

2.3. Preparation of CS/WS_2 aerogels

The CS/WS_2 dispersion was immersed in 1 M NaOH at room temperature for 24 h to get the dark green hydrogels. The hydrogels were washed with ultrapure water for several times to remove NaOH, and then freeze-dried in a freeze dryer (Alpha 2–4, Christ, Germany) at 0.12 bar (absolute pressure) for 24 h. The obtained aerogels were abbreviated as CS/WS_2 aerogels. As control, aerogels without WS_2 nanosheets (abbreviated as CS) were also prepared.

2.4. Adsorption experiments

Typically, known amounts of adsorbents (i.e., CS and CS/WS_2 aerogels) were immersed into 10 mL of metallic salt solution (e.g., Pb^{2+}, Cu^{2+}, and Cd^{2+}) with different concentrations and shaken at 150 rpm certain time and temperatures. The pH values were ranging from 1.0 to 5.0, and the initial concentrations of Pb^{2+} were ranging from 7.5 to 115 μg/mL. Then, the solution was filtered through a PES membrane (0.22 μm), and the adsorption amounts of metallic ions were calculated by the changes of solution concentrations (measured by an atomic absorption spectrophotometer, WFX-130B, China). All the experiments were conducted in triplicates, and the relative errors were within 5%. The adsorption capacities of heavy metal ions on per unit mass of adsorbent were calculated according the following equations:

$$q_e = \frac{(C_0 - C_e)V}{m} \tag{1}$$

$$q_t = \frac{(C_0 - C_t)V}{m} \tag{2}$$

where q_e (mg/L) and q_t (mg/L) were the adsorption quantities at saturation and specific time (min), C_e (mg/L) and C_t (mg/L) were the concentrations of metallic ions at saturation and specific time (min), C_0 (mg/L) and v (L) were the initial concentration and volume of metallic salt solution, and m (g) was the weight of sample.

The adsorption desorption cycle experiment was performed to evaluate the reusability of aerogel. During the desorption process, the aerogel loaded Pb^{2+} was soaked into 0.2 M EDTA-2Na solution. And the aerogel was washed several times at certain temperature. Subsequently, the aerogel was immersed in distilled water to remove residual solution and freeze dried 12 h. And the adsorption and regeneration were further repeated for five cycles.

2.5. Characterization

The microstructures of samples were analyzed by using a Hitachi H-7650 transmission electron microscope (TEM, Japan) and a Quanta 250 field emission environmental scanning electron microscope (FE-SEM, USA). UV-Vis spectrophotometric analyses were performed on a U2910 UV-Vis spectrophotometer (Hitachi, Japan). Fourier-transform infrared spectroscopy (FT-IR) were recorded by a FT-IR micro infrared spectrometer (Nicolet 5700, U.S.) in the wavenumber ranging from 4,000 to 500 cm^{-1}. Raman spectra were measured by a Raman spectrometer (LabRAM HR Evolution, France). X-ray diffraction (XRD) patterns were recorded on a D8 Advance X-ray diffractometer (Bruker, Germany). The surface chemistry of samples was analyzed by a PhI 5000 VersaProbe X-ray photoelectron spectroscopy (XPS) system (UIVAC-PHI, Japan) equipped with an Al Kα (hv = 1,486.6 eV) X-ray source. Curve-fitting analysis of the XPS data was performed using MultiPak 9.3. All spectra were calibrated following the standard C1s binding energy (284.8 eV) and the curve-fitting was performed using the Gauss-Lorentz method. Thermal properties of samples were evaluated with a thermogravimetric (TG) analyzer (NETZSCH STA409PC, USA). The samples were heated under dry nitrogen purge (a flow rate of 10 mL/min) from room temperature to 1,000°C (a ramp rate of 10°C/min). The specific surface areas and pore sizes of aerogels were measured by nitrogen adsorption apparatus (Micromeritics, AsAp2020, USA). The mechanical properties of aerogels were characterized using an electron universal testing machine (Jinan Tianchen Testing Machine Manufacturing Co., Ltd).

3. Results and discussion

3.1. Preparation and characterization of aerogels

Chitosan possessed plenty of functional groups (e.g., –OH and –NH_2) that can stably bound to the surfaces of transition metal dichalcogenides nanosheets (TMDNs) *via* noncovalent interactions (e.g., H-bond and electrostatic attraction), facilitate the layer-by-layer liquid-phase exfoliation of TMDNs under ultrasonic, and hinder the restacking and aggregation of as-exfoliated TMDNs by forming stable hybrids (Fig. 1A) [23]. Taking WS_2 as an example, after sonicating in the solution of chitosan followed by removal of unexfoliated bulk WS_2, the dispersion of nanoscale WS_2 with color of dark green was obtained (Fig. S1). Ultraviolet-visible (UV-Vis) spectroscopy was employed to evaluate the exfoliation efficiency of TMDNs in the presence of CS. Comparing with the negligible absorption of bulk WS_2 and CS, the absorption peak at ~630 nm of CS/WS_2 dispersion may imply the presence of exfoliated WS_2 (Fig. S2). The concentrations of CS solutions and ultrasonic time seemed to be two dominated factors that affected the exfoliation efficiency of WS_2. As shown in Fig. 1B and C, the absorption intensity at 630 nm were enhanced with the increase of chitosan concentrations, and reached a maximum at an initial chitosan concentration of ~20 mg/mL. Further increasing the concentrations of chitosan resulted in declined exfoliation efficiency, which might be ascribed to the improved viscosities of solutions (Fig. S3) [24]. In addition, the exfoliation amount of WS_2 progressively increased and reached an equilibrium at ≈7 h (Fig. 1D and Fig. S4).

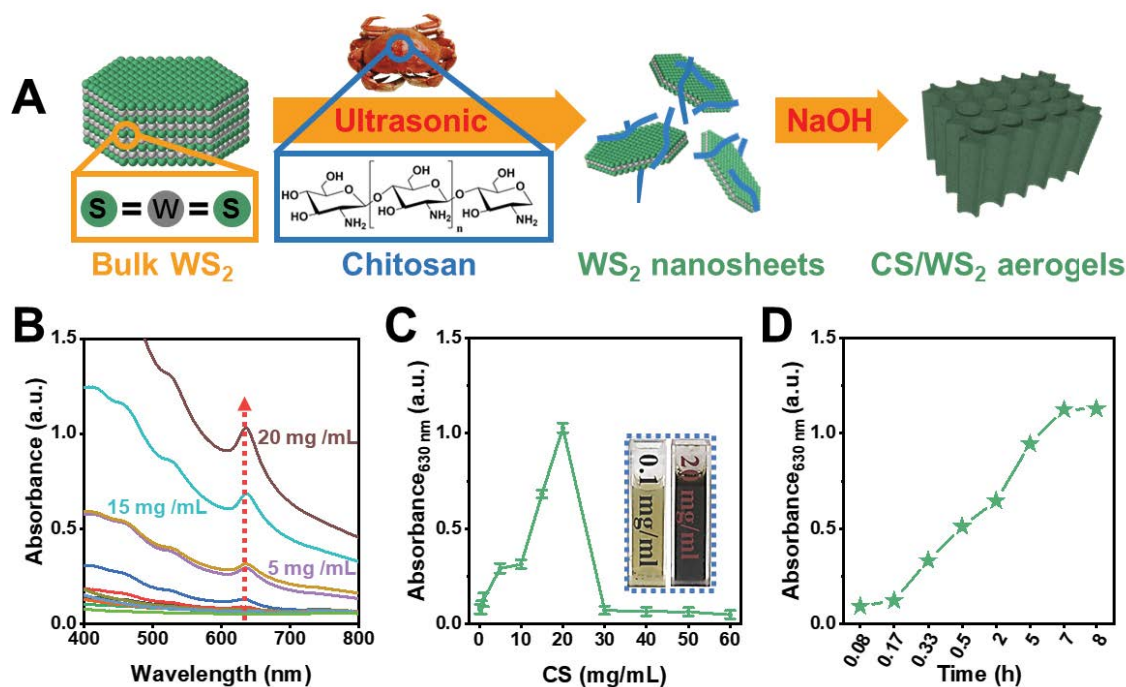The exfoliated WS_2 exhibited typical two-dimensional sheet-like morphology, and the homogeneous

Fig. 1. (A) Schematic illustration of the liquid-phase exfoliation of WS_2 nanosheets and the preparation of CS/WS_2 aerogels. (B) UV-Vis spectra and (C) UV-Vis absorption at 630 nm of the dispersions of WS_2 nanosheets exfoliated under different CS concentrations (ultrasonic for 10 h). The optical images were set as insets. (D) UV-Vis absorption at 630 nm of the dispersions of WS_2 nanosheets exfoliated in 20 mg/mL CS solution for different ultrasonic times.

contrast suggested the nanosheets were mono- or multi-layers (Figs. 2A and B) [25]. Typically, polymer assisted liquid-phase exfoliation of transition metal dichalcogenides nanosheets was ascribed to the noncovalent interactions (e.g., H-bond and electrostatic attraction) between them [26]. As presented in Fig. 2C, the CS/WS$_2$ hybrids exhibited characteristic peaks of CS at 3,444 cm^{-1} (–OH and –NH$_2$ stretching vibrations), 2,925 cm^{-1} (–CH stretching vibration in –CH and –CH$_2$), 1,603 cm^{-1} (–NH$_2$ bending vibration), 1,380 cm^{-1} (–CH symmetric bending vibration in –CHOH–), 1,080 and 1,027 cm^{-1} (–CO stretching vibration in –CONH) in their FT-IR spectra, indicated the presence of CS on the surfaces of WS$_2$ nanosheets [27]. Besides, a distinct red shift from 1,603 cm^{-1} (CS/WS$_2$) to 1,598 cm^{-1} (WS$_2$) was observed in partially enlarged FT-IR spectra, implied the variations of chemical environments around –NH$_2$ in CS and the potential H-bond between CS and WS$_2$ (Fig. 2D). The X-ray photoelectron survey spectrum (XPS) of CS/WS$_2$ demonstrated the characteristic peaks of O1s, N1s, C1s, S2p, and W4f, indicated the presence of both CS and WS$_2$ in these composite aerogels (Fig. 2E). Fig. 2F presented the high-resolution S2p spectra of CS and CS/WS$_2$ hybrids, in which the binding energies at around 161.8 and 163.0 eV, corresponded to S2p$_{2/3}$ and S2p$_{1/2}$ components of WS$_2$, shifted to higher values (162.6 and 163.7 eV) in CS/WS$_2$ hybrids, also implied the potential H-bond between –NH$_2$ and –OH of CS and S atom of WS$_2$ (Fig. 2G). Anyway, these strong interactions made CS stably bond to the surfaces of WS$_2$, and facilitated their efficient liquid-phase exfoliation [28].

Chitosan can form hydrogels *via* phase inversion processes, during which the protonated chitosan was easily deprotonated by alkali, and cross-linked into hydrogels.

As shown in Fig. 3A, the dark green CS/WS$_2$ aerogels were obtained by NaOH triggered crosslinking, water exchange, and freeze-drying processes. The uniform crosslinking networks in CS/WS$_2$ aerogels and the according element mapping images of S, W, and C were observed by SEM, indicating the successful compositing of chitosan and WS$_2$ nanosheets (Fig. S5). The presence of CS and WS$_2$ nanosheets in CS/WS$_2$ aerogels can be further verified by Raman spectra and XRD patterns. The Raman spectrum of CS exhibited no obvious Raman bands in the case of visible region excitation, and the new peaks at 351 and 420 cm^{-1}, assigned to the A$_{1g}$ and E$_{2g}$ photon modes of WS$_2$ showed up in CS/WS$_2$ aerogels [29,30], demonstrating the presence of WS$_2$ nanosheets in hybrid aerogels (Fig. S6). The CS/WS$_2$ aerogels displayed both characteristic patterns of CS (10.8° for crystal I and 20.1° for crystal II) [31] and WS$_2$ (14.4° for the layer-packing diffraction) [32], also indicating the successful compositing of these two components (Fig. S7).

To be noted, unlike pure CS aerogels that with uneven and dense micro cross-linked structures (Fig. S8), the CS/WS$_2$ aerogels possessed highly porous and honeycomb-like micro network morphologies (Fig. 3B–D). Such hierarchical microstructures might be ascribed to the potential co-assembly behavior of WS$_2$ nanosheets and CS that triggered by the noncovalent H-bond interactions. As rigid two dimensional nanocomponents, WS$_2$ nanosheets joined the crosslinking process of CS, which resulted in the formation of oriented micro channels along with the anisotropic growth of ice crystals. The WS$_2$ nanosheets endowed CS/WS$_2$ aerogels with enhanced deformability under compression, as the compressive stress of CS/WS$_2$ was greater than that of CS under same strain conditions (Fig. 3E). In addition, the
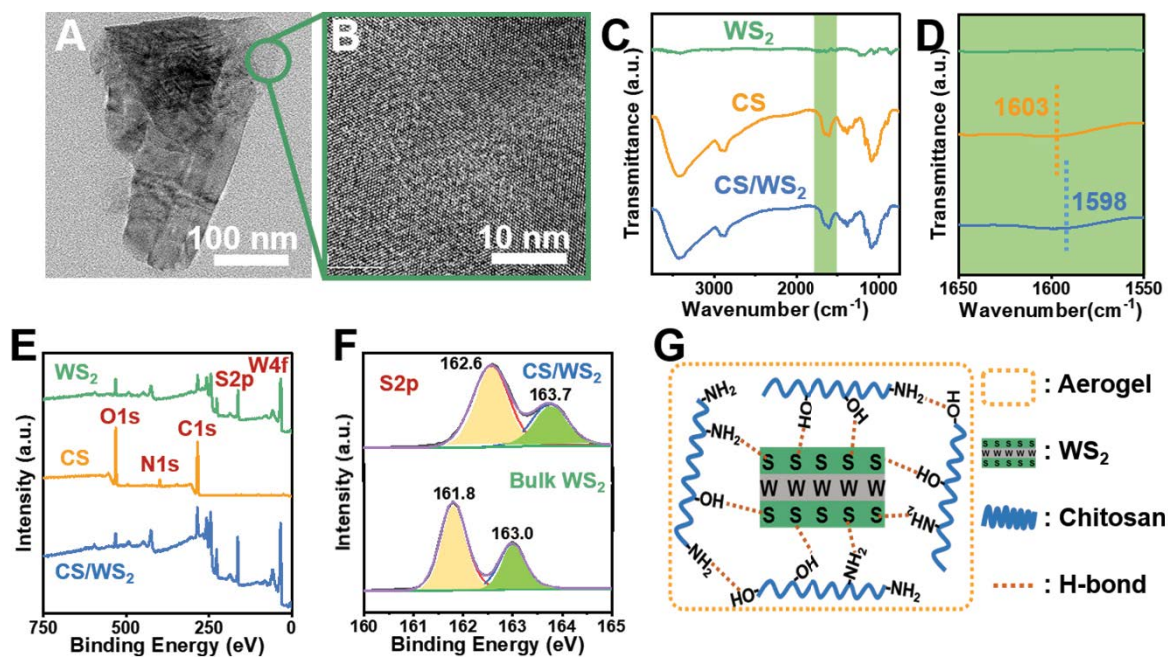

Fig. 2. (A,B) Transmission electron microscopy (TEM) images of exfoliated WS$_2$ nanosheets. (C) FT-IR spectra and (D) magnified FT-IR spectra (ranging from 1,650 to 1,550 cm^{-1}) of WS$_2$, CS, and CS/WS$_2$ hybrids. (E) XPS survey spectra of WS$_2$, CS, and CS/WS$_2$ hybrids. (F) S2p spectra of bulk WS$_2$ and CS/WS$_2$ hybrids. (G) Schematic illustration of the potential H-bonding interactions between WS$_2$ and CS.
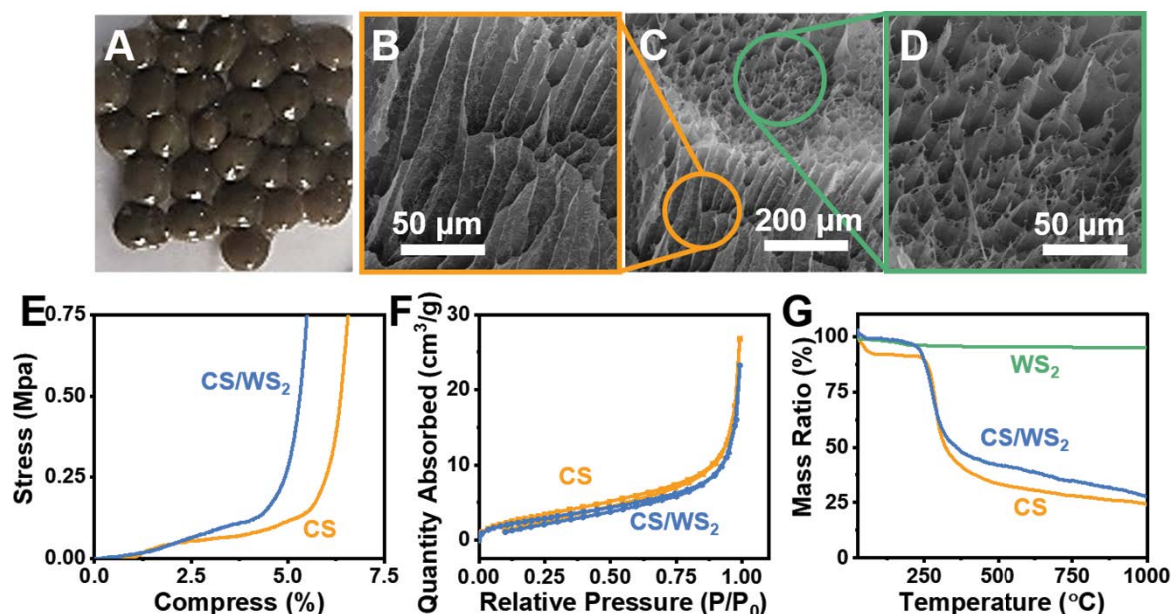
Fig. 3. (A) Optical photograph and SEM images (B,D) of CS/WS$_2$ aerogels. (E) Compression performance and (F) BET isotherms of CS/WS$_2$ aerogels and CS aerogels. (G) Thermogravimetric curves of WS$_2$, CS aerogels, and CS/WS$_2$ aerogels.

co-assembly of chitosan and WS$_2$ nanosheets exhibited negligible effects on the nitrogen adsorption isotherms properties of aerogels, and their pore sizes slightly declined (Fig. 3F and Table S1). The presence of thermal stable WS$_2$ nanosheets (only a small weight loss even heating up to 1,000°C) in composite aerogels also slightly improved the thermal stabilities of CS/WS$_2$ aerogels, which can be seen in the TG analysis (Fig. 3G).

3.2. Adsorption study

3.2.1. Effect of adsorbent dosage and pH on adsorption

Benefiting from the anisotropic co-assembled micro structures, as well as the specific and strong interactions between WS$_2$ and Pb^{2+}, the CS/WS$_2$ aerogels exhibited superior adsorption performance toward Pb^{2+}. When the initial concentration of Pb^{2+} was 100 μg/mL, pH = 5, and the dosage of aerogels was 1 mg/10 mL, the CS/WS$_2$ aerogels presented superior adsorption performance (~206 mg/g) than pure CS aerogels (~63 mg/g), which might be ascribed to the denser adsorption sites (i.e., sulfur atoms on the surface of WS$_2$ nanosheets) [33]. However, the adsorption capacity decreased with more adsorbents used due to the large number of unoccupied adsorption sites (Fig. 4A). Besides the dosages of adsorbents, pH values of systems were also dominated factors on the removal efficiency of Pb^{2+} (Fig. 4B). Obviously, low pH values were negative to the adsorption of Pb^{2+} by CS/WS$_2$ aerogels (206.5 mg/g at pH = 5.0, and 13.8 mg/g at pH = 1.0), which might be ascribed to the competition between H$^+$ and heavy metal ions in the interactions with Pb^{2+}, as well as the structural deformation of aerogels in low pH [34]. The CS/WS$_2$ aerogel displayed a pH$_{zpc}$ value at around 3.3, beyond which the negative charged adsorbents facilitated their electrostatic attraction with Pb^{2+}, and exhibited higher adsorption capacity

(Fig. S9). However, when the pH values were beyond 5.0, hydroxide precipitations occurred due to the hydrolysis of Pb^{2+}. Above all, the dosage of adsorbents and the pH value were fixed at 1 mg and 5 for further researches.

3.2.2. Adsorption kinetics

Adsorption kinetics was one of the key points to evaluate the performance of adsorbents, for which the rapid response was very important for wastewater treatment [35]. As depicted in Fig. 4C, the Pb^{2+} were rapidly adsorbed by CS/WS$_2$ aerogels in the first 120 min, then the adsorption rates slowed down and reached equilibrium in the following time. The equilibrium adsorption capacities for Pb^{2+} were 44.88, 99.09, 226.97 mg/g, corresponding to the initial concentrations of Pb^{2+} at 50, 75, and 100 μg/mL, respectively. The date was further simulated with the pseudo-first-order and pseudo-second-order kinetic models according to the following equations.

$$\ln\left(q_e - q_t\right) = \ln q_e - k_1 t \tag{3}$$

$$\frac{t}{q_t} = \frac{1}{\left(k_2 q_e^2\right)} + \frac{t}{q_e} \tag{4}$$

where q_t and q_e represented the adsorption capacities (mg/g) at the time t and adsorption equilibrium; k_1 (min^{-1}) and k_2 (mg/g min) were rate constants of the pseudo-first-order and pseudo-second-order adsorption, respectively.

Fig. 4D and E and Table S2 show the adsorption kinetic plots of Pb^{2+} adsorption on the surfaces of CS/WS$_2$ aerogels. The fitting result of pseudo-second-order kinetic model ($R^2 > 0.99$) was better than that of the pseudo-first-order kinetic model ($R^2 > 0.82$), indicated that the adsorption of

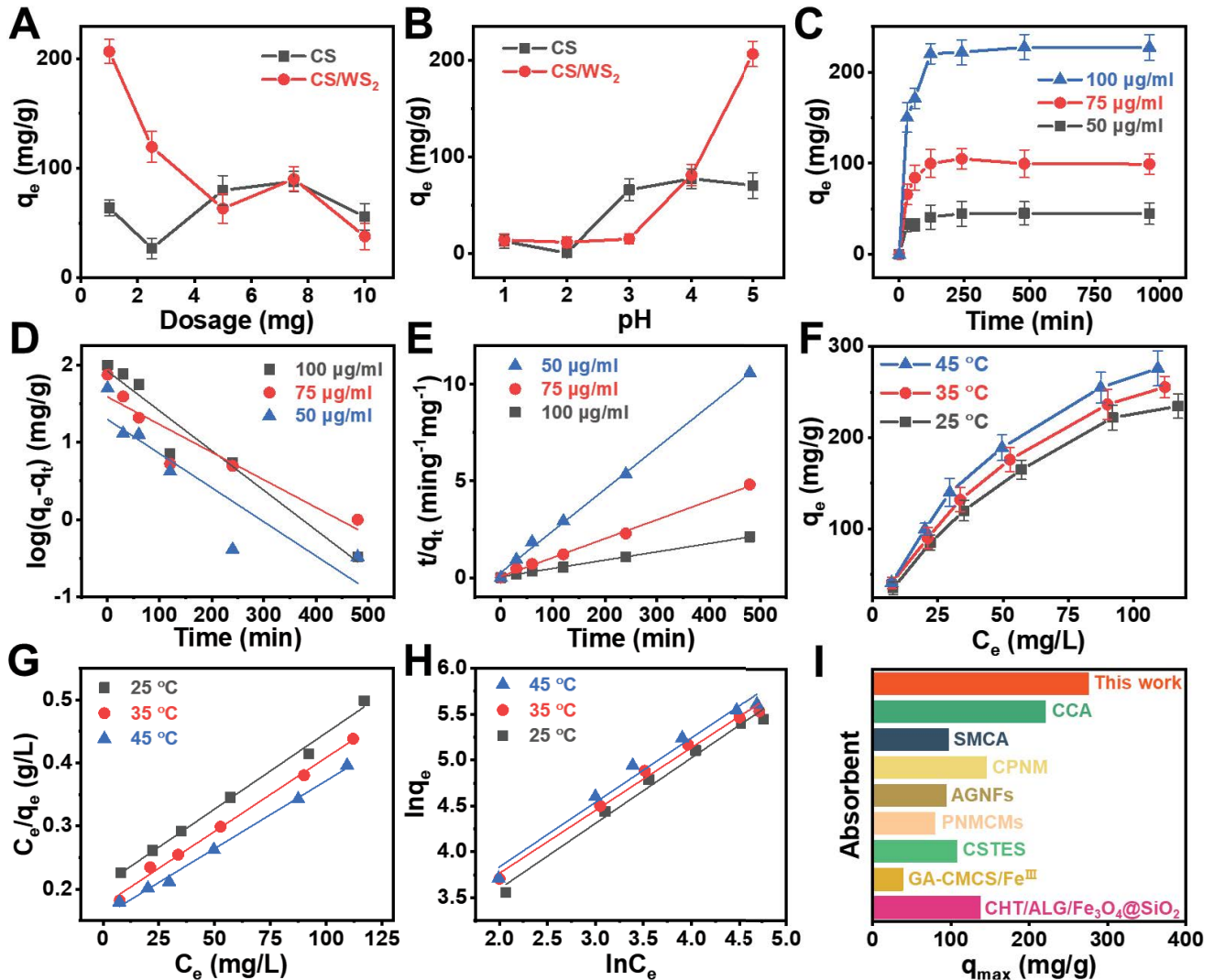Fig. 4. Effects of (A) adsorbent dosage and (B) pH on the adsorption capacities of Pb^{2+} by CS and CS/WS$_2$ aerogels. (C) Effect of contact time on the adsorption of Pb^{2+} on CS/WS$_2$ aerogels. (D) Pseudo-first-order and (E) pseudo-second-order kinetic models for the adsorption of Pb^{2+} by CS/WS$_2$ aerogels. (F) Equilibrium isotherms of Pb^{2+} adsorption on CS/WS$_2$ aerogels. (G) Langmuir isotherm model. (H) Freundlich isotherm model. (I) Comparison of the adsorption performance of CS/WS$_2$ aerogels with other chitosan-based aerogels for Pb^{2+} adsorption. (Experimental conditions: (A) pH = 5, C_0 = 100 µg/mL, T = 25°C, t = 24 h; (B) adsorbent dosage = 0.1 g/L, C_0 = 100 µg/mL, T = 25°C, t = 24 h; (C) pH = 5, adsorbent dosage = 0.1 g/L, T = 25°C, t = 24 h; (F) pH = 5, adsorbent dosage = 0.1 g/L, C_0 = 100 µg/mL, t = 24 h).

Pb^{2+} by CS/WS$_2$ aerogels was mainly controlled by chemical interactions [36]. In addition, the adsorption isotherms were also evaluated to study the migration of Pb^{2+} from aqueous solution to the surfaces of CS/WS$_2$ aerogels [37]. The adsorption performances at different temperatures (25°C, 35°C, and 45°C) and initial concentrations (100 µg/mL) of Pb^{2+} were recorded and fitted into the linearized Langmuir and Freundlich isotherm models as follows (Fig. 4F–H):

$$\frac{C_e}{q_e} = \frac{C_e}{q_m} + \frac{1}{K_L q_m} \tag{5}$$

$$\ln q_e = \ln K_F + \left(\frac{1}{n}\right) \ln C_e \tag{6}$$

where C_e represented the equilibrium concentration (mg/L); q_e was the equilibrium adsorption capacity (mg/g); q_m represented the maximal adsorption capacity (mg/g) under experimental conditions; K_L, K_F and n were the relative model constants.

The calculated parameters derived from the two models are listed in Table S3. The higher correlation coefficient of Langmuir model (R^2 > 0.99) than Freundlich model (R^2 > 0.97) indicated a monolayer adsorption mechanism of Pb^{2+} onto the surfaces of CS/WS$_2$ aerogels [38]. The high number of available adsorption sites on the surfaces of CS/WS$_2$ aerogels endowed them a maximum adsorption capacity of ~275.9 mg/g, which was higher than many other chitosan-based adsorbents reported in literatures (Fig. 4I and Table S5). The thermodynamic parameters, such as changes

in standard Gibbs free energy ($\Delta G°$), enthalpy change ($\Delta H°$), and entropy change ($\Delta S°$) of Pb^{2+} adsorption by CS/WS$_2$ aerogels were further determined as follows [9]:

$$\ln K_d = \frac{\Delta S°}{R} + \frac{-\Delta H°}{RT} \tag{7}$$

$$K_d = \frac{(C_0 - C_e)V}{mC_e} \tag{8}$$

$$\Delta G° = -RT \ln K_d \tag{9}$$

where R (J/mol·K) was the gas constant, m (g) was the adsorbent dosage, K_d was the distribution coefficient and T (K) was the absolute solution temperature.

The values of $\Delta H°$ and $\Delta S°$ were calculated according to the slope and intercept of the plots of $\ln K_d$ vs. $1/T$ (Fig. S10 and Table S4). The positive value of $\Delta H°$ indicated that the adsorption process of Pb^{2+} was endothermic, meanwhile the positive entropy change ($\Delta S°$) implied an increase in randomness at the interface between CS/WS$_2$ aerogels and heavy metal ions [39]. Gibbs free energy was a thermodynamic function to determine the direction of reaction, and the decrease in $\Delta S°$ values at higher temperatures demonstrated that the adsorption process was autogenic [40]. All these results indicated that the adsorption of Pb^{2+} on the surfaces of CS/WS$_2$ aerogels were spontaneous and endothermic.

3.2.3. Co-existing metal ions

Thanks to the specific Lewis acid-base soft-soft interactions between Pb^{2+} and S atoms in WS$_2$ nanosheets, as well as the oriented porous structure in the aerogels that can improve the diffusion rate of heavy metal ions, the CS/WS$_2$ aerogels also displayed promising selectivity toward Pb^{2+} even in the presence of co-existing metal ions (e.g., Cu^{2+} and Cd^{2+}). As shown in Fig. S11, when the Cu^{2+} and Cd^{2+} were added in the solution of Pb^{2+}, the adsorption capacity of CS/WS$_2$ aerogels toward Pb^{2+} decreased due to the competition from external metal ions. However, the adsorption of Pb^{2+} was still higher than $Cu^{2+}$and Cd^{2+}, which maintained ~54% of their maximal adsorption capacity, suggested promising selectivity of CS/WS$_2$ aerogels toward Pb^{2+}. Besides, the aerogels also presented promising reusability, that their adsorption capability toward Pb^{2+} still maintained ~90% of the maximal uptake after 5 cycles (Fig. S12).

3.3. Adsorption mechanism

To further study the adsorption mechanism of Pb^{2+} by CS/WS$_2$ aerogels, the XPS analysis of aerogels before and after Pb^{2+} adsorption was conducted. Fig. S13 shows that
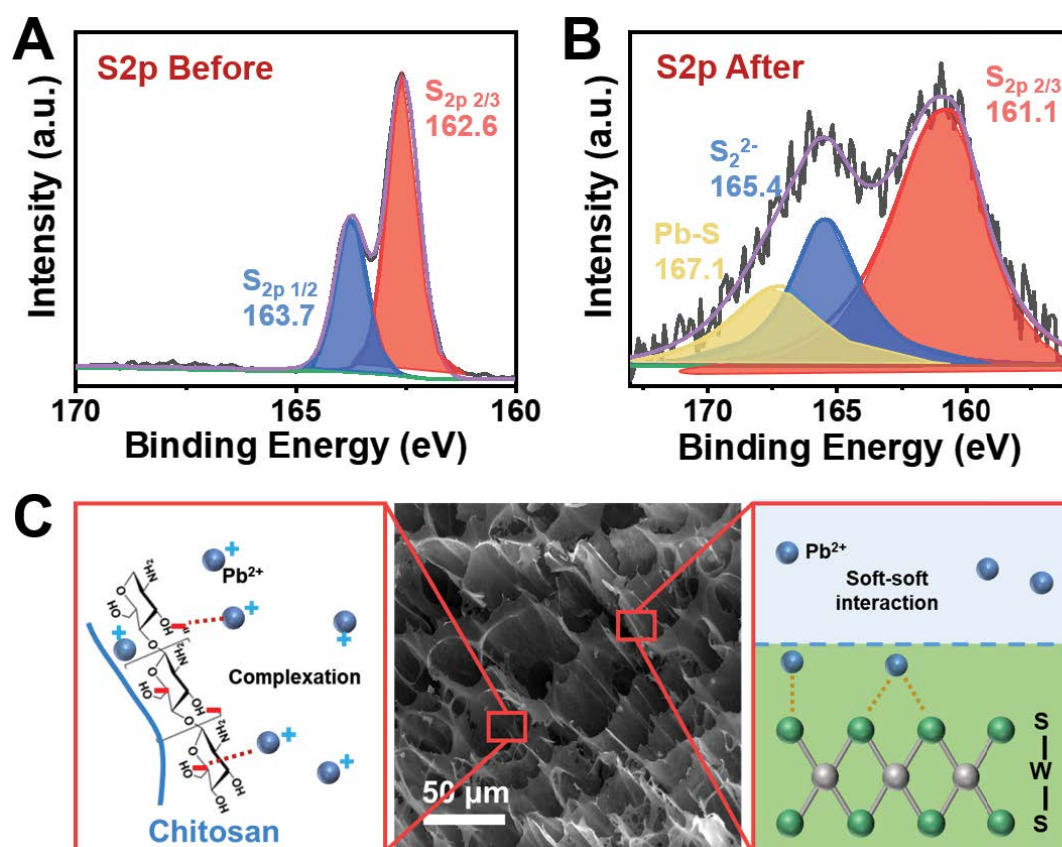

Fig. 5. High-resolution S2p XPS spectra of CS/WS$_2$ aerogels before (A) and after (B) Pb^{2+} adsorption. (C) Schematic illustration of the potential Pb^{2+} adsorption mechanism on the surfaces of CS/WS$_2$ aerogels.

new peaks attributed to the binding energy of Pb4f occurred in aerogels after the adsorption of Pb^{2+}, confirming the successful capture of Pb^{2+} by CS/WS_2 aerogels [41]. The binding energy peaks at around 162.6 eV (S^{2-}) and 163.7 eV (S^{2-}) in the S2p spectrum of CS/WS_2 aerogels shifted to 161.1 and 165.4 eV after adsorption, indicated the potential Lewis acid-base soft-soft interactions between sulfur atoms and Pb^{2+} (Fig. 5A and B) [42,43]. Besides, after Pb^{2+} adsorption, a new peak assigned to Pb–S was observed at ~167.1 eV, implied the formation of Pb–S species *via* strong interactions between Pb^{2+} and sulfur atoms in CS/WS_2 aerogels [44,45]. The O1s spectrum of chitosan showed a peak at 532.2 eV (Fig. S14A), which was probably derived from C–OH. However, a new peak at 531.3 eV after Pb^{2+} adsorption due to the formation of metal oxide bonds (Pb–O bond), indicating the oxygen-containing group in chitosan also facilitated the removal of Pb^{2+} by chemisorption (Fig. S14B) [46]. In conclusion, the adsorption of Pb^{2+} on the surfaces of CS/WS_2 aerogels might be ascribed to a synergistic effect between CS and WS_2 nanosheets, which mainly included the strong soft-soft interaction between Pb^{2+} and S atoms in WS_2, as well as their complexation with O atoms in chitosan, as described in Fig. 5C.

4. Conclusions

In summary, chitosan was applied as assistant agent for the liquid-phase exfoliation of WS_2 nanosheets and the construction of composite aerogels (CS/WS_2) *via* co-assembly processes. With the help of interactions between CS and WS_2 nanosheets (e.g., H-bond), the CS/WS_2 aerogels with oriented microchannel structures were obtained and applied for the removal of Pb^{2+} from wastewater. Owing to the three-dimensional anisotropic porous structures and sulfur-rich surfaces, the CS/WS_2 aerogels exhibited superior Pb^{2+} adsorption performance (275.9 mg/g) than many other chitosan-based adsorbents reported in the literatures. Besides, the adsorption of Pb^{2+} by CS/WS_2 aerogels were also rapid (reached an equilibrium at ~120 min) and selective (maintained ~54% of the maximal Pb^{2+} uptake). In this way, an eco-friendly TMDNs-based composite aerogels with promising and selective adsorption performance toward Pb^{2+} was obtained *via* a simple and green way.

Acknowledgements

Associated content

Supporting information available: photograph and UV-Vis absorption of the WS_2 nanosheets dispersion, optical and SEM images of CS, Raman shifts, XRD patterns, XPS survey spectra, porous properties of the composite aerogels, and the detailed parameters of fitted adsorption curves.

Declaration of competing interest

The authors declare that they have no known competing financial interests or personal relationships that could have appeared to influence the work reported in this paper.

References

[1] L. Cai, D. Ying, X. Liang, M. Zhu, X. Lin, Q. Xu, Z. Cai, X. Xu, L. Zhang, A novel cationic polyelectrolyte microsphere for ultrafast and ultra-efficient removal of heavy metal ions and dyes, Chem. Eng. J., 410 (2021) 128404, doi: 10.1016/j.cej.2021.128404.

[2] A. Dhakshinamoorthy, A.M. Asiri, H. Garcia, 2D metal-organic frameworks as multifunctional materials in heterogeneous catalysis and electro/photocatalysis, Adv. Mater., 31 (2019) 1900617, doi: 10.1002/adma.201900617.

[3] E. Nazlabadi, E. Karamati Niaragh, M.R.A. Moghaddam, A systematic and critical review of two decades' application of response surface methodology in biological wastewater treatment processes, Desal. Water Treat., 228 (2021) 92–120.

[4] L. Qiu, J. Zhang, Z. Guo, W. Liu, Asymmetric superwetting stainless steel meshes for on-demand and highly effective oil-water emulsion separation, Sep. Purif. Technol., 273 (2021) 118994, doi: 10.1016/j.seppur.2021.118994.

[5] J.M. Monteagudo, A. Durán, V. Valderas, X. Chen, X. Shi, Capture of ambient air CO_2 from municipal wastewater mineralization by using an ion-exchange membrane, Sci. Total Environ., 790 (2021) 148136, doi: 10.1016/j.scitotenv.2021.148136.

[6] H.-J. Hong, J. Ryu, Synthesis of copper nanoparticles from Cu^{2+}-spiked wastewater via adsorptive separation and subsequent chemical reduction, Nanomaterials, 11 (2021) 2051, doi: 10.3390/nano11082051.

[7] Y. Shang, X. Xu, B. Gao, S. Wang, X. Duan, Single-atom catalysis in advanced oxidation processes for environmental remediation, Chem. Soc. Rev., 50 (2021) 5281–5322.

[8] M. Massoudinejad, A. Asadi, M. Vosoughi, M. Gholami, B. Kakavandi, M.A. Karami, A comprehensive study (kinetic, thermodynamic and equilibrium) of arsenic(V) adsorption using $KMnO_4$ modified clinoptilolite, Korean J. Chem. Eng., 32 (2015) 2078–2086.

[9] M. Omidinasab, N. Rahbar, M. Ahmadi, B. Kakavandi, F. Ghanbari, G.Z. Kyzas, S.S. Martinez, N. Jaafarzadeh, Removal of vanadium and palladium ions by adsorption onto magnetic chitosan nanoparticles, Environ. Sci. Pollut. Res., 25 (2018) 34262–34276.

[10] B. Kakavandi, A. Raofi, S.M. Peyghambarzadeh, B. Ramavandi, M.H. Niri, M. Ahmadi, Efficient adsorption of cobalt on chemical modified activated carbon: characterization, optimization and modeling studies, Desal. Water Treat., 111 (2018) 310–321.

[11] R. Rezaei Kalantry, A. Jonidi Jafari, A. Esrafili, B. Kakavandi, A. Gholizadeh, A. Azari, Optimization and evaluation of reactive dye adsorption on magnetic composite of activated carbon and iron oxide, Desal. Water Treat., 57 (2016) 6411–6422.

[12] J. Salimi, B. Kakavandi, A.A. Babaei, A. Takdastan, N. Alavi, A. Neisi, B. Ayoubi-Feiz, Modeling and optimization of nonylphenol removal from contaminated water media using a magnetic recoverable composite by artificial neural networks, Water Sci. Technol., 75 (2017) 1761–1775.

[13] A.A. Babaei, A. Azari, R.R. Kalantary, B. Kakavandi, Enhanced removal of nitrate from water using nZVI@MWCNTs composite: synthesis, kinetics and mechanism of reduction, Water Sci. Technol., 72 (2015) 1988–1999.

[14] Z. Wang, B. Mi, Environmental applications of 2D molybdenum disulfide (MoS_2) nanosheets, Environ. Sci. Technol., 51 (2017) 8229–8244.

[15] Z. Wang, A. Sim, J.J. Urban, B. Mi, Removal and recovery of heavy metal ions by two-dimensional MoS_2 nanosheets: performance and mechanisms, Environ. Sci. Technol., 52 (2018) 9741–9748.

[16] K. Ai, C. Ruan, M. Shen, L. Lu, MoS_2 nanosheets with widened interlayer spacing for high-efficiency removal of mercury in aquatic systems, Adv. Funct. Mater., 26 (2016) 5542–5549.

[17] H. Sim, J. Lee, B. Park, S.J. Kim, S. Kang, W. Ryu, S.C. Jun, High-concentration dispersions of exfoliated MoS_2 sheets stabilized by freeze-dried silk fibroin powder, Nano Res., 9 (2016) 1709–1722.

[18] E.P. Ferreira-Neto, S. Ullah, T.C. da Silva, R.R. Domeneguetti, A.P. Perissinotto, F.S. de Vicente, U.P. Rodrigues-Filho,

A.P. Perissinotto, Bacterial nanocellulose/MoS$_2$ hybrid aerogels as bifunctional adsorbent/photocatalyst membranes for in-flow water decontamination, ACS Appl. Mater. Interfaces, 12 (2020) 41627–41643.

[19] S. Fan, J. Chen, C. Fan, G. Chen, S. Liu, H. Zhou, R. Liu, Y. Zhang, H. Hu, Z. Huang, Y. Qin, J. Liang, Fabrication of a CO$_2$-responsive chitosan aerogel as an effective adsorbent for the adsorption and desorption of heavy metal ions, J. Hazard. Mater., 416 (2021) 126225, doi: 10.1016/j.jhazmat.2021.126225.

[20] A. Li, R. Lin, C. Lin, B. He, T. Zheng, L. Lu, Y. Cao, An environment-friendly and multi-functional absorbent from chitosan for organic pollutants and heavy metal ion, Carbohydr. Polym., 148 (2016) 272–280.

[21] W. Wang, J. Niu, J. Guo, L. Yin, H. Huang, In situ synthesis of PPy-FexOy-CTS nanostructured gel membrane for highly efficient solar steam generation, Sol. Energy Mater. Sol. Cells, 201 (2019) 110046, doi: 10.1016/j.solmat.2019.110046.

[22] J. Zhang, Y. Wang, D. Liang, Z. Xiao, Y. Xie, J. Li, Sulfhydryl-modified chitosan aerogel for the adsorption of heavy metal ions and organic dyes, Ind. Eng. Chem. Res., 59 (2020) 14531–14536.

[23] Q. Liu, Q. Peng, C. Ma, M. Jiang, L. Zong, J. Zhang, Efficient transition metal dichalcogenides exfoliation by cellulose nanocrystals for ultrabroad-pH/temp stable aqueous dispersions and multi-responsive photonic films, Chem. Eng. J., 428 (2022) 132594, doi: 10.1016/j.cej.2021.132594.

[24] L. Zong, M. Li, C. Li, Bioinspired coupling of inorganic layered nanomaterials with marine polysaccharides for efficient aqueous exfoliation and smart actuating hybrids, Adv. Mater., 29 (2017) 1604691, doi: 10.1002/adma.201604691.

[25] F. Huang, J. Jian, R. Wu, Few-layer thick WS$_2$ nanosheets produced by intercalation/exfoliation route, J. Mater. Sci., 51 (2016) 10160–10165.

[26] J. You, L. Zhu, Z. Wang, L. Zong, M. Li, X. Wu, C. Li, Liquid exfoliated chitin nanofibrils for re-dispersibility and hybridization of two-dimensional nanomaterials, Chem. Eng. J., 344 (2018) 498–505.

[27] A.M. Ahmed, M.I. Ayad, M.A. Eledkawy, M.A. Darweesh, E.M. Elmelegy, Removal of iron, zinc, and nickel-ions using nano bentonite and its applications on power station wastewater, Heliyon, 7 (2021) e06315, doi: 10.1016/j.heliyon.2021.e06315.

[28] Y. Li, X. Liu, Z. Zhang, S. Zhao, G. Tian, J. Zheng, D. Wang, S. Shi, T.P. Russell, Adaptive structured pickering emulsions and porous materials based on cellulose nanocrystal surfactants, Angew. Chem. Int. Ed., 57 (2018) 13560–13564.

[29] A.S. Estrada-Montaño, D Espinobarro-Velázquez, M. Sauzameda, E. Terrazas, R. Reyes-Martinez, D. Lardi-zábal, L.A. Manjarrez-Nevárez, G. Zaragoza-Galan, Photo-luminescence in non-conjugated polyelectrolyte films containing 7-hydroxy-flavylium cation, Polym. Bull., 77 (2020) 5051–5063.

[30] A. Falin, M. Holwill, H. Lv, W. Gan, J. Cheng, R. Zhang, D. Qian, M.R. Barnett, E.J.G. Santos, K.S. Novoselov, T. Tao, X. Wu, L.H. Li, Mechanical properties of atomically thin tungsten dichalcogenides: WS$_2$, WSe$_2$, and WTe$_2$, ACS Nano, 15 (2021) 2600–2610.

[31] L. Lv, N. Chen, C. Feng, Y. Gao, M. Li, Xanthate-modified magnetic chitosan/poly(vinyl alcohol) adsorbent: preparation, characterization, and performance of Pb(II) removal from aqueous solution, J. Taiwan Inst. Chem. Eng., 790 (2017) 148136, doi: 10.1016/j.jtice.2017.06.009.

[32] M. Xiong, J. Qian, K. Yang, Z. Chen, T. Mei, J. Wang, J. Li, L. Yu, X. Wang, Efficient polysulfide anchor: brain coral-like WS$_2$ nanosheets, J. Mater. Sci., 55 (2020) 12031–12040.

[33] J. Tang, Y. Li, X. Wang, M. Daroch, Effective adsorption of aqueous Pb^{2+} by dried biomass of *Landoltia punctata* and *Spirodela polyrhiza*, J. Cleaner Prod., 145 (2017) 25–34.

[34] Z. Li, W. Kang, N. Wei, J. Qiu, C. Sun, B. Cheng, Preparation of a polyvinylidene fluoride tree-like nanofiber mat loaded with manganese dioxide for highly efficient lead adsorption, RSC Adv., 7 (2017) 8220–8229.

[35] L. Yang, Y. Zhan, Y. Gong, E. Ren, J. Lan, R. Guo, B. Yan, S. Chen, S. Lin, Development of eco-friendly CO$_2$-responsive cellulose nanofibril aerogels as "green" adsorbents for anionic dyes removal, J. Hazard. Mater., 405 (2021) 124194, doi: 10.1016/j.jhazmat.2020.124194.

[36] S. Chen, Y. Huang, X. Han, Z. Wu, C. Lai, J. Wang, Q. Deng, Z. Zeng, S. Deng, Simultaneous and efficient removal of Cr(VI) and methyl orange on LDHs decorated porous carbons, Chem. Eng. J., 352 (2018) 306–315.

[37] K.C. Kang, J.H. Ju, S.S. Kim, M.H. Baik, S.W. Rhee, Sorption of aqueous Pb^{2+} ion on synthetic manganese oxides-intercalated with exchangeable cations, J. Ind. Eng. Chem., 17 (2011) 565–569.

[38] S. Raza, X. Yong, M. Raza, J. Deng, Synthesis of biomass trans-anethole based magnetic hollow polymer particles and their applications as renewable adsorbent, Chem. Eng. J., 352 (2018) 20–28.

[39] C. Luo, J. Wang, P. Jia, Y. Liu, J. An, B. Cao, K. Pan, Hierarchically structured polyacrylonitrile nanofiber mat as highly efficient lead adsorbent for water treatment, Chem. Eng. J., 262 (2015) 775–784.

[40] J. Wang, K. Pan, Q. He, B. Cao, Polyacrylonitrile/polypyrrole core/shell nanofiber mat for the removal of hexavalent chromium from aqueous solution, J. Hazard. Mater., 244–245 (2013) 121–129.

[41] C. Gao, X.-L. Wang, Q.-D. An, Z.-Y. Xiao, S.-R. Zhai, Synergistic preparation of modified alginate aerogel with melamine/chitosan for efficiently selective adsorption of lead ions, Carbohydr. Polym., 256 (2021) 117564, doi: 10.1016/j.carbpol.2020.117564.

[42] L. Zou, R. Qu, H. Gao, X. Guan, X. Qi, C. Liu, Z. Zhang, X. Lei, MoS$_2$/RGO hybrids prepared by a hydrothermal route as a highly efficient T catalytic for sonocatalytic degradation of methylene blue, Results Phys., 14 (2019) 102458, doi: 10.1016/j.rinp.2019.102458.

[43] C. Ding, F. Liu, Y. Zhang, S. Hayase, T. Masuda, R. Wang, Y. Zhou, Y. Yao, Z. Zou, Q. Shen, Passivation strategy of reducing both electron and hole trap states for achieving high-efficiency PbS quantum-dot solar cells with power conversion efficiency over 12%, ACS Energy Lett., 5 (2020) 3224–3236.

[44] B. Adilbekova, Y. Lin, E. Yengel, H. Faber, G. Harrison, A. El-Labban, D.H. Anjum, V. Tung, T.D. Anthopoulos, Liquid-phase exfoliation of MoS$_2$ and WS$_2$ in aqueous ammonia and their application in highly efficient organic solar cells, J. Mater Chem. C, 8 (2020) 5259–5264.

[45] M.-J. Choi, Oh. J, J.-K. Yoo, J. Choi, D.M. Sim, Y.S. Jung, Tailoring of the PbS/metal interface in colloidal quantum dot solar cells for improvements of performance and air stability, Energy Environ. Sci., 7 (2014) 3052–3060.

[46] L. Kong, Z. Li, X. Huang, S. Huang, H. Sun, M. Liu, L. Li, Efficient removal of Pb(II) from water using magnetic Fe$_3$S$_4$ / reduced graphene oxide composites, J. Mater. Chem. A, 5 (2017) 19333–19342.

Supporting information

Fig. S1. Photograph of the aqueous dispersion of WS$_2$ nanosheets.
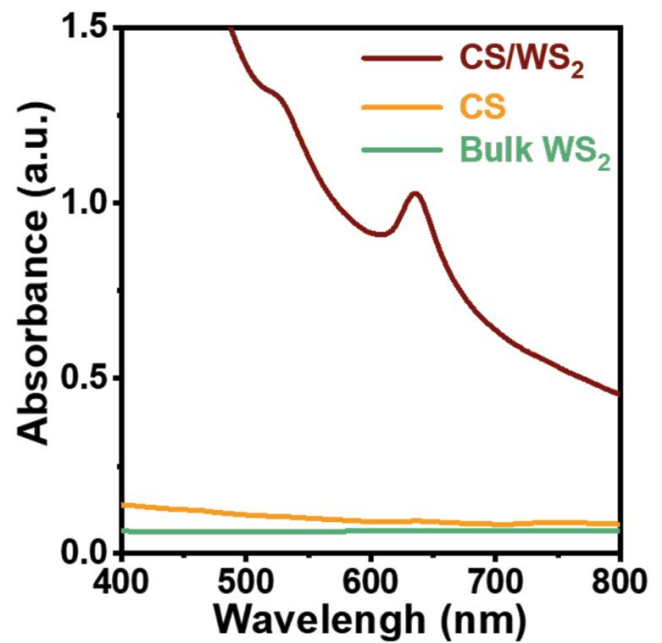
Fig. S2. UV-Vis spectra of CS, bulk WS$_2$ and CS/WS$_2$ dispersions.

Fig. S3. Optical images of the dispersions of WS$_2$ nanosheets exfoliated at different chitosan concentrations for 10 h sonication.
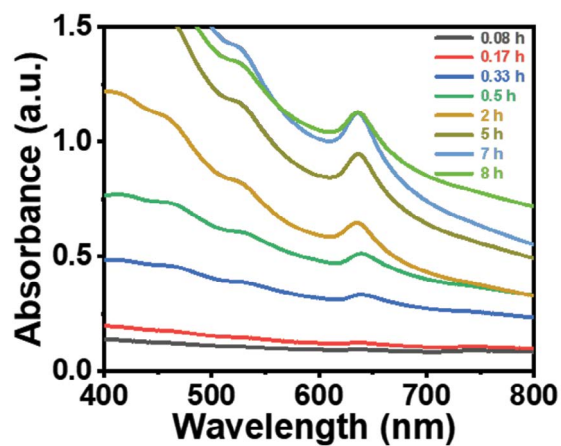
Fig. S4. UV-Vis spectra of the dispersions of WS$_2$ nanosheets exfoliated in 20 mg/mL chitosan solution for different ultrasonic times.
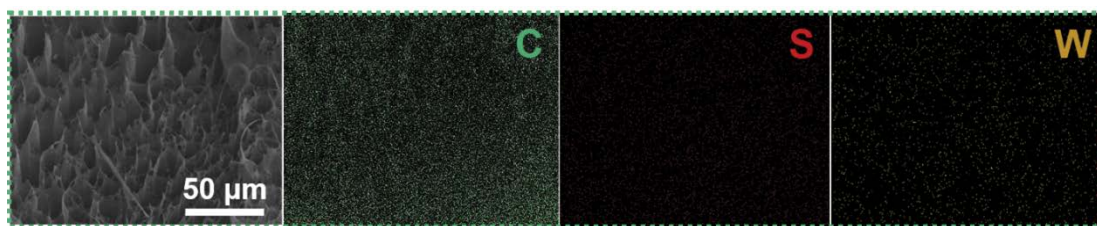
Fig. S5. Energy-dispersive X-ray spectroscopy mapping images of CS/WS$_2$ aerogels.
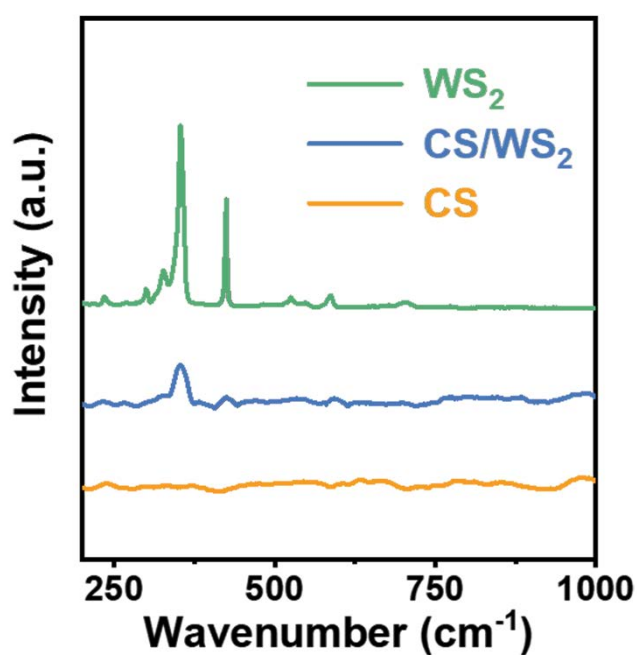
Fig. S6. Raman spectra of CS, bulk WS$_2$ and CS/WS$_2$ hybrids.
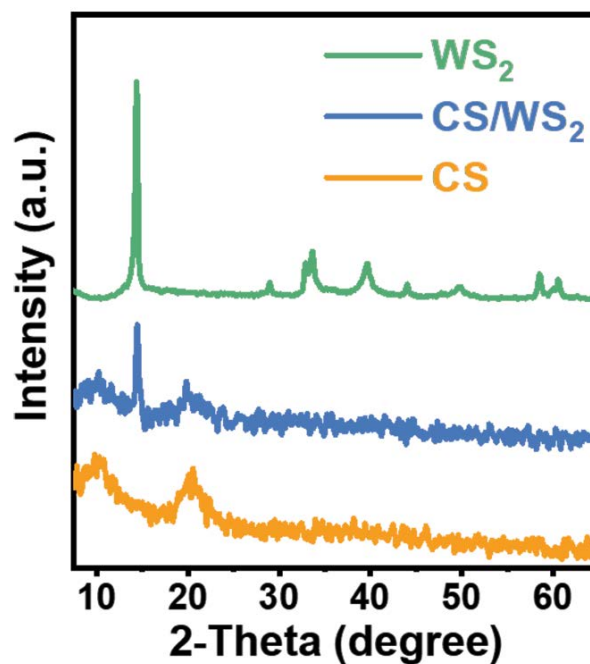
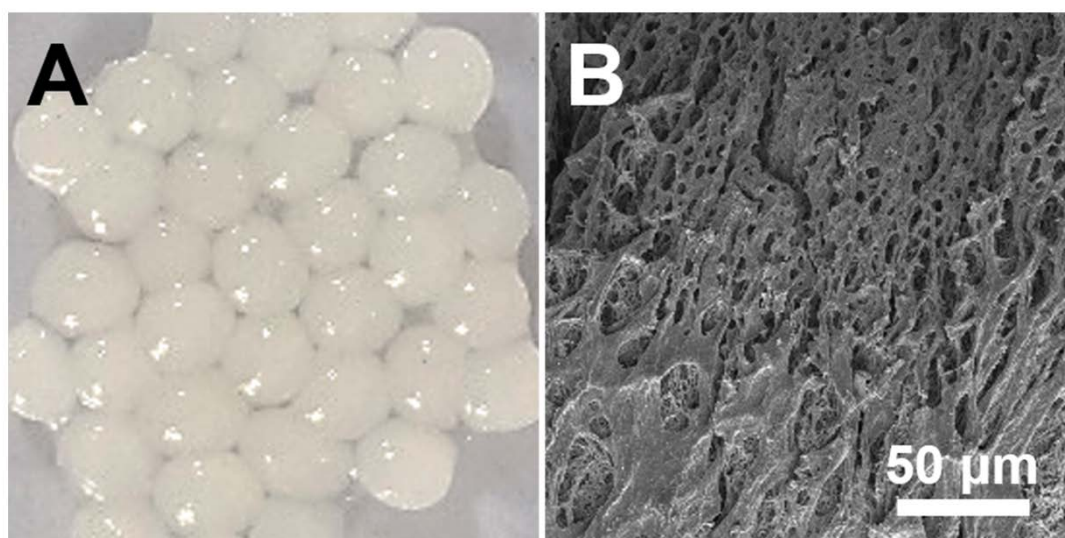Fig. S7. XRD patterns of CS, bulk WS$_2$ and CS/WS$_2$ hybrids.

Fig. S8. (A) Optical photograph and (B) SEM image of pure CS aerogels.

Table S1
Porous properties of as-synthesized CS aerogels and CS/WS$_2$ aerogels

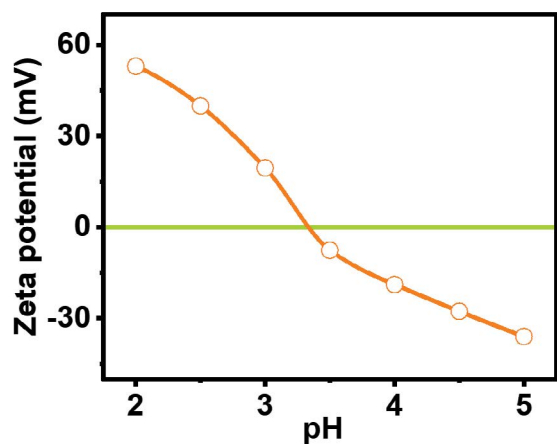|	Surface area (m²/g)	Pore size (nm)
CS aerogels	12.44	13.05
CS/WS$_2$ aerogels	10.47	13.30

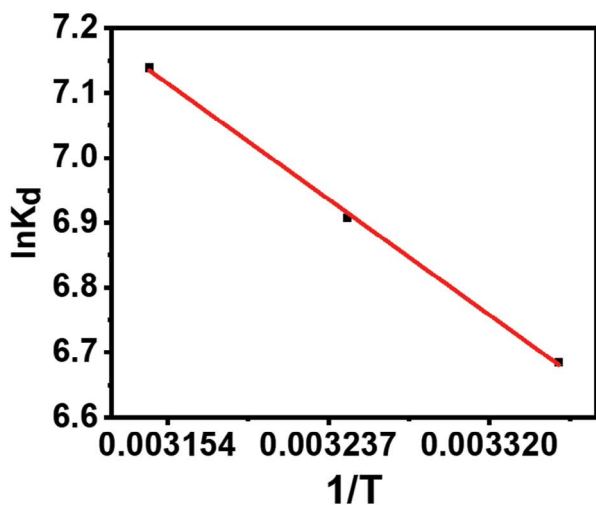Fig. S9. Zeta potentials of CS/WS$_2$ under different pH values.

Fig. S10. Van't Hoff plot for the adsorption of Pb^{2+} on CS/WS$_2$ aerogels.

Table S3
Parameters of the Langmuir and Freundlich isotherms models for Pb^{2+} adsorption on CS/WS$_2$ aerogels

Temperature (°C)	Langmuir model			Freundlich model		
	q_m (mg/g)	b (L/mg)	R^2	K_F (mg/g)	$1/n$	R^2
25	413.22	0.206	0.993	8.74	0.7142	0.9839
35	427.35	0.174	0.9994	10.98	0.6847	0.9889
45	465.12	0.157	0.995	11.37	0.7029	0.9741

Table S4
Thermodynamic parameters of Pb^{2+} adsorption on CS/WS$_2$ aerogels

Temperature (K)	$\Delta G°$ (kJ/mol)	$\Delta H°$ (kJ/mol)	$\Delta S°$ (J/mol·K)
298	−16.56	–	–
308	−17.69	17.878	115.539
318	−18.87	–	–

Table S5
Comparison of the adsorption performance of CS/WS$_2$ aerogels with other chitosan based materials for Pb^{2+} adsorption

Absorbent	q_{max} (mg/g)	References
Chitosan/cellulose sulfate	137.8	[S1]
Sulfhydryl chitosan/sodium alginate	38.87	[S2]
Chitosan/poly(ethylene oxide) nanofibres	108	[S3]
Fe$_3$O$_4$/CS NPs	79.24	[S4]
Amine-grafted chitosan nanofibers (AGNFs)	94.34	[S5]
CSTEC fiber	144.93	[S6]
CMCh/gallic acid/FeIII	97.15	[S7]
Chitosan/alginate/Fe$_3$O$_4$@SiO$_2$	220.68	[S8]
Chitosan/WS$_2$	275.9	This work

Table S2
Parameters of the pseudo-first-order and pseudo-second-order models for Pb^{2+} adsorption on CS/WS$_2$ aerogels

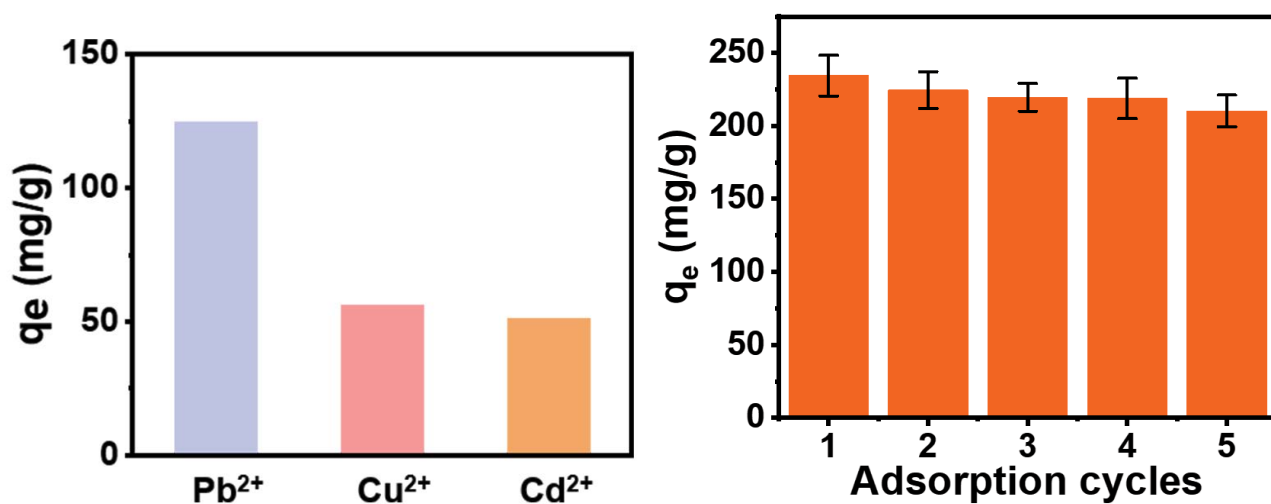| C_0 (mg/L)	$q_{e,exp}$	Pseudo-first-order model			Pseudo-second-order model		
		k_1 (1/min)	$q_{e,cal}$ (mg/g)	R^2	k_2 (g/mg·min)	$q_{e,cal}$ (mg/g)	R^2
50	45.29	0.0044	3.654	0.8206	1.74×10^{-3}	46.43	0.9978
75	105.04	0.0036	4.893	0.8717	1.57×10^{-3}	102.15	0.9975
100	227.30	0.0051	6.819	0.9447	3.93×10^{-4}	232.02	0.9983

Fig. S11. Effects of co-existing metal ions on the adsorption of Pb^{2+} on CS/WS$_2$ aerogels.

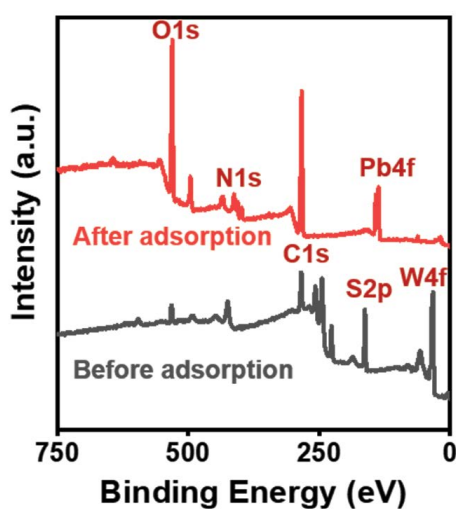Fig. S12. Adsorption capability of CS/WS$_2$ aerogels in recycling adsorbing Pb^{2+}.

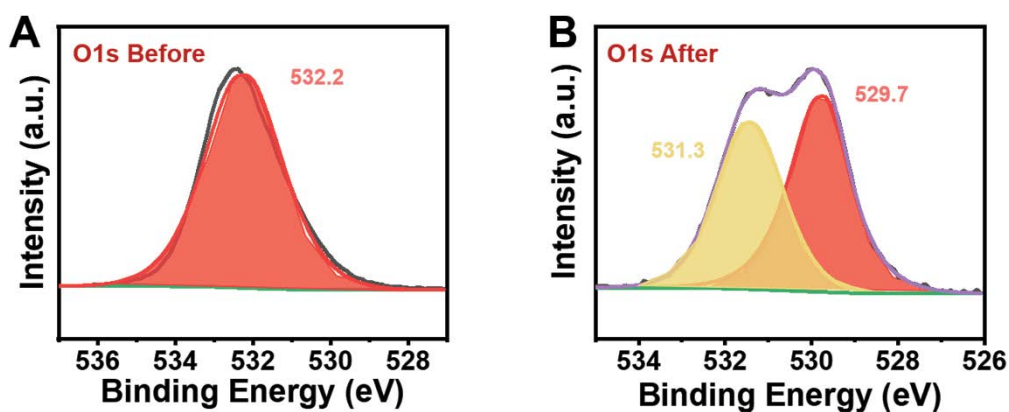Fig. S13. Total XPS survey spectra of CS/WS$_2$ aerogels before and after the adsorption of Pb^{2+}.

Fig. S14. O1s XPS spectra of CS/WS$_2$ aerogels before (A) and after (B) Pb^{2+} adsorption.

References

[S1] S. Najaflou, M.F. Rad, M. Baghdadi, G.R. Nabi Bidhendi, Removal of Pb(II) from contaminated waters using cellulose sulfate/chitosan aerogel: equilibrium, kinetics, and thermodynamic studies, J. Environ. Manage., 286 (2021) 112167, doi: 10.1016/j.jenvman.2021.112167.

[S2] J. Zhang, Y. Wang, D. Liang, Z. Xiao, Y. Xie, J. Li, Sulfhydryl-modified chitosan aerogel for the adsorption of heavy metal ions and organic dyes, Ind. Eng. Chem. Res., 59 (2020) 14531–14536.

[S3] M.I. Shariful, S.B. Sharif, J.J.L. Lee, U. Habiba, B.C. Ang, M.A. Amalina, Adsorption of divalent heavy metal ion by mesoporous-high surface area chitosan/poly(ethylene oxide) nanofibrous membrane, Carbohydr. Polym., 157 (2017) 57–64.

[S4] H.-L. Fan, S.-F. Zhou, W.-Z. Jiao, G.-S. Qi, Y.-Z. Liu, Removal of heavy metal ions by magnetic chitosan nanoparticles prepared continuously via high-gravity reactive precipitation method, Carbohydr. Polym., 174 (2017) 1192–1200.

[S5] S. Haider, F.A.A. Ali, A. Haider, W.A. Al-Masry, Y. Al-Zeghayer, Novel route for amine grafting to chitosan electrospun nanofibers membrane for the removal of copper and lead ions from aqueous medium, Carbohydr. Polym., 199 (2018) 406–414.

[S6] Y. Niu, K. Li, D. Ying, Y. Wang, J. Jia, Novel recyclable adsorbent for the removal of copper(II) and lead(II) from aqueous solution, Bioresour. Technol., 229 (2017) 63–68.

[S7] J. Yang, M. Li, Y. Wang, H. Wu, N. Ji, L. Dai, Y. Li, L. Xiong, R. Shi, Q. Sun, High-strength physically multi-cross-linked chitosan hydrogels and aerogels for removing heavy-metal ions, J. Agric. Food Chem., 67 (2019) 13648–13657.

[S8] D.P. Facchi, A.L. Cazetta, E.A. Canesin, V.C. Almeida, E.G. Bonafé, M.J. Kipper, A.F. Martins, New magnetic chitosan/alginate/Fe_3O_4@SiO_2 hydrogel composites applied for removal of Pb(II) ions from aqueous systems, Chem. Eng. J., 337 (2018) 595–608.